ADVANCED MATERIALS
www.advmat.de

Lysosome-Targeting Protein Degradation Through Endocytosis Pathway Triggered by Polyvalent Nano-Chimera for AD Therapy

*Xiaorong Wang, Shiqin Chen, Xue Xia, Yufan Du, Ya Wei, Wenqin Yang, Yiwei Zhang, Yujun Song, Ting Lei, Qianqian Huang, and Huile Gao**

The excessive up-regulation of receptor for advanced glycation end products (RAGE), a well-known pathological marker, drives the onset and progression of Alzheimer's disease. Although lysosome-targeting protein degradation has emerged as an effective therapeutic modality, the limited lysosome-sorting efficacy greatly hindered the degradation efficiency of target proteins. Herein, a lysosome-shuttle-like nano-chimera (endoTAC) is proposed based on polyvalent receptor binding mode for enhanced RAGE degradation as well as precise drug delivery. The endoTAC shows a high affinity to RAGE and enhances RAGE degradation due to its polyvalent-interaction with RAGE. Additionally, endoTAC features increased accumulation in diseased brain and shows promise as a precise brain delivery system. After loading with simvastatin, the SV@endoTAC proves to successfully reverse pathological features both in vitro and in vivo. The work proposes that the combination of a lysosome-targeting chimera and an effective drug delivery system can be promising in Alzheimer's disease therapy.

1. Introduction

Alzheimer's disease (AD) is a progressive neurodegenerative disorder that affects the brain, gradually impairing memory, thinking, and behavior.[1] It is the most common cause of dementia, accounting for 60–70% of all cases.[2] There is currently no cure for AD, with only few treatments available to help manage symptoms.[3] Research is now in full swing to investigate the underlying mechanisms of the disease and to further slow its progression or prevent it altogether.[4] One emerging hypothesis is that the dysfunction of the blood-brain barrier (BBB) has been intimately implicated in the pathogenesis of AD.[5] Various well-known AD pathologies can compromise the integrity of BBB, leading to its dysfunction, with the upregulated advanced glycosylation end product-specific receptor (RAGE) serving as a prominent marker.[6] Furthermore, pathologically high-expressed RAGE on the BBB binds to β amyloid (Aβ) in the peripheral circulatory system and facilitates Aβ influx, thereby exacerbating the accumulation of Aβ in the brain. In addition, the interaction between RAGE and Aβ triggers the downstream nuclear factor-κB (NF-κB) inflammatory pathway, leading to intracellular oxidative stress and neuronal malfunction, which ultimately results in neuroinflammation and neurodegeneration. All of these continue to undermine the integrity of BBB and encourage the deterioration of AD. Therefore, targeting RAGE may represent a potential therapeutic strategy to protect the BBB and prevent AD progression.

Nowadays, targeted protein degradation (TPD) strategy opens up new avenues for handling various undruggable targets, and a multitude of lysosome-based degraders have been developed to degrade extracellular proteins, transmembrane proteins, and various protein aggregates, with a focus on how to improve the efficacy of lysosomal sorting of proteins of interest (POIs).[7] Recently, most advances have attempted to engage various lysosome-trafficking receptors (LTRs) for protein depletion. For example, the integrin, scavenger receptors, and the cation-independent mannose-6-phosphate receptor have all been utilized to construct lysosome-targeting chimeras (LYTACs).[8] Apart from these endeavors depending on LTRs,[9] recent investigations reveal that the binding mode between the ligand and receptor dictates the efficacy of POI sorting into lysosomes.[10] The polyvalent binding pattern, characterized by the concurrent binding of multiple ligands and receptors, serves as a key determinant in augmenting the affinity and specificity of receptor–ligand interactions across various biological processes, encompassing antibody-antigen recognition, virus–cell interactions, and cell–cell recognition.[11] Distinct binding modes between transferrin and its receptor have been shown to be implicated in cellular transport of transferrin, ultimately affecting transferrin expression. Specifically, transferrin is

X. Wang, S. Chen, X. Xia, Y. Du, Y. Wei, W. Yang, Y. Zhang, Y. Song, T. Lei, Q. Huang, H. Gao
Key Laboratory of Drug-Targeting and Drug Delivery System of the Education Ministry and Sichuan Province
Sichuan Engineering Laboratory for Plant-Sourced Drug and Sichuan Research Center for Drug Precision Industrial Technology
West China School of Pharmacy
Sichuan University
Chengdu 610041, China
E-mail: gaohuile@scu.edu.cn

The ORCID identification number(s) for the author(s) of this article can be found under https://doi.org/10.1002/adma.202411061

DOI: 10.1002/adma.202411061

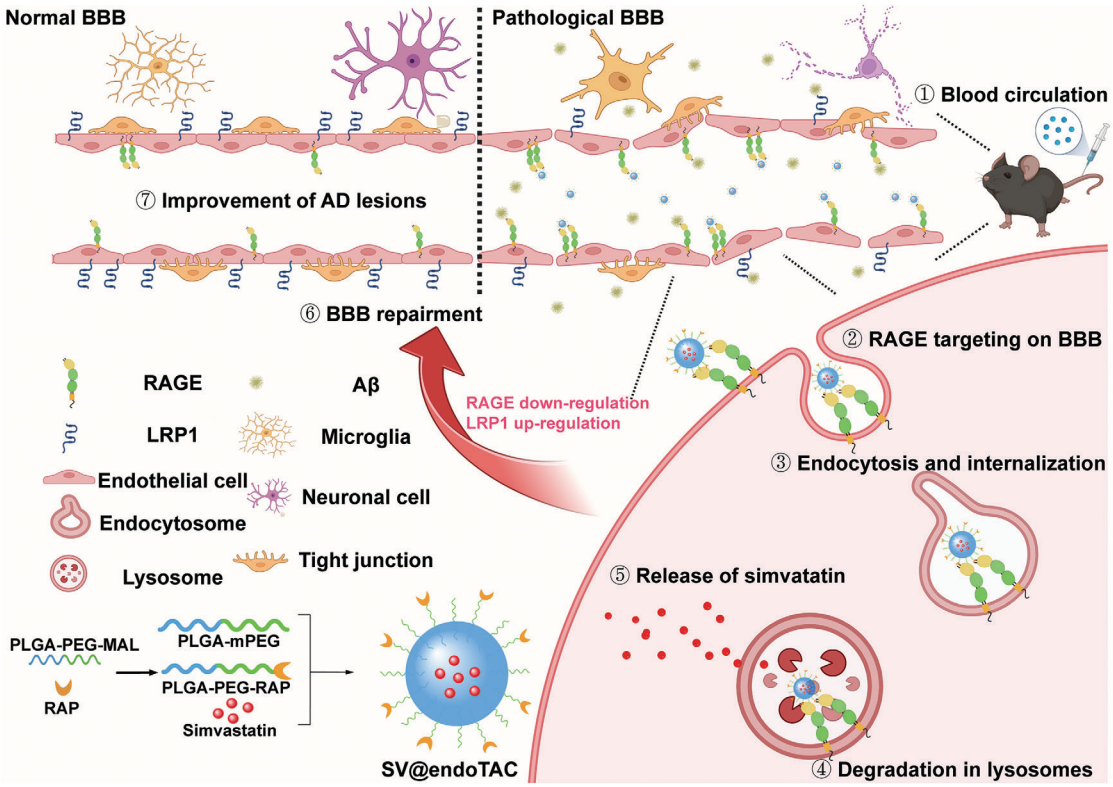

Scheme 1. Diagram depicting the combination of a lysosome-shuttle-like protein degrader and an effective drug delivery system (SV@endoTAC) for AD therapy. (Created with http://biorender.com/).

preferentially targeted for lysosomal breakdown when it is polyvalently attached to its receptors.[12] Accordingly, it is plausible to posit that the development of modular ligands capable of multivalent binding to RAGE may result in the effective degradation of RAGE through enhanced lysosomal sorting efficiency. Hence, a lysosomal-shuttling nano-chimera (endoTAC) was engineered, incorporating the peptide RAP (ELKVLMEKEL) onto nanomaterials to enable the polyvalent ligand–receptor interactions.[13] This design may enhance the affinity between the ligands and receptors, thereby facilitating augmented degradation of RAGE. Moreover, given the strong affinity between RAP and RAGE, the degrader could selectively accumulate at the compromised BBB and function as a precise drug delivery platform for lesion-specific targeting, enabling the delivery of diverse therapeutic agents.

Considering the intricate pathogenesis of AD, combination therapy targeting multiple factors is believed to be more efficacious. In the context of BBB injury, a notable reduction in low-density lipoprotein receptor-related protein 1 (LRP1) levels was observed alongside aberrantly high-expressed RAGE levels. LRP1 serves a crucial function in facilitating the efflux of Aβ from the brain;[6a,14] hence, diminished LRP1 levels lead to Aβ accumulation in the brain—a process associated with prevalent genetic susceptibility factors for AD, including apolipoprotein E4 and phosphatidylinositol-binding clathrin assembly.[15] Additionally, the reduced expression of LRP1 is closely correlated with BBB impairment, tau protein propagation, and neuronal degeneration.[5a,16] Therefore, simvastatin,[17] a pharmaceutical agent known to upregulate the LRP1, was incorporated into endoTAC for the combined treatment of AD.

To sum up, a lysosomal- shuttle-like nano-chimera with precise targeting ability was fabricated and subsequently loaded with simvastatin (SV@endoTAC) for AD therapy. The SV@endoTAC exhibited a robust binding affinity with RAGE on the compromised BBB through polyvalent interaction between RAP and RAGE, enabling enhanced sorting of RAGE into lysosomes for degradation. Concurrently, the released simvastatin from the formulation facilitated the up-regulation of LRP1. By restoring BBB integrity via RAGE down-regulation and LRP1 up-regulation, the SV@endoTAC actively modulated Aβ transport, reduced Aβ deposition in the brain, attenuated neuroinflammation and oxidative stress, supported neuronal recovery, and rectified brain homeostatic disorders, offering a multi-faceted therapeutic strategy for AD (**Scheme 1**).

2. Results and Discussion

2.1. Preparation and Characterization of Nanoparticles

RAP was connected with $PLGA_{5000}$-PEG_{2000}-MAL to obtain $PLGA_{5000}$-PEG_{2000}-RAP (PPR), the result of the matrix-assisted laser desorption/ionization time of flight mass spectrometry (MALDI TOF-MS) and ^{1}H-nuclear magnetic resonance spectroscopy (^{1}H-NMR) confirmed the successful synthesis of PPR (Figures S1 and S2, Supporting Information). The commercially available bEnd.3 cells overexpressing RAGE (abbreviated

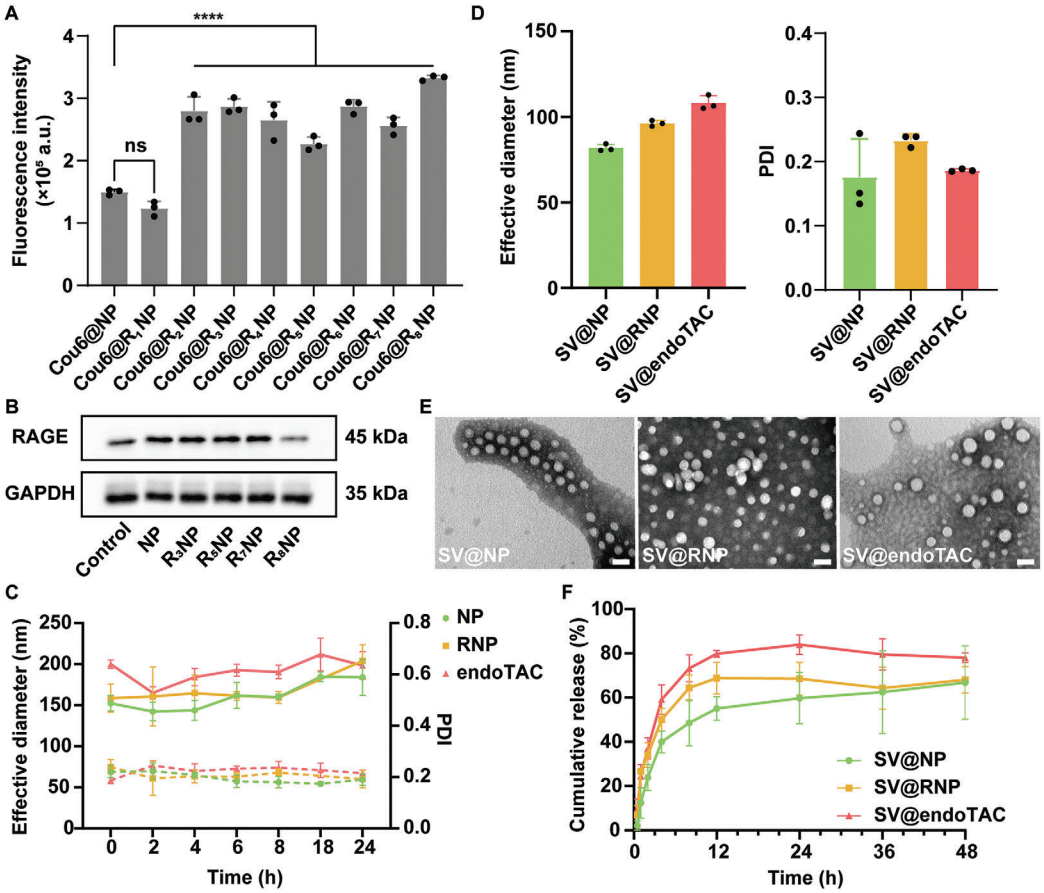

Figure 1. Characterization of nanoparticles. A) Uptake of nanoparticles measured by flow cytometry after incubated with bEnd.3-RAGE cells for 0.5 h. B) Western blot of RAGE on bEnd.3-RAGE cells after incubated with R_nNP for 24 h. C) Changes in effective particle size (solid lines) and PDI (dotted lines) of nanoparticles incubated with 50% FBS. D) The effective particle size and PDI of simvastatin-loaded nanoparticles. E) TEM images of simvastatin-loaded nanoparticles. Scale bar represents 40 nm. F) Release of simvastatin from nanoparticles in vitro. Data are presented as mean ± SD ($n = 3$). Statistical differences were analyzed by one-way ANOVA Dunnett's test, ns means no significant, $^{****}p < 0.0001$.

to bEnd.3-RAGE cells) was used for RAGE-related experiments to better simulate AD pathology (Figure S3, Supporting Information), and further incubated with 5 μM A$\beta_{1\text{-}42}$ oligomer after multiple generations to reduce the effect of decreased RAGE expression (Figure S4, Supporting Information).

Herein, coumarin-6 (Cou6) labeled nanoparticles were used to perform related cellular experiments. Nanoparticles modified with RAP in different proportions (R_nNP) were prepared to assess their ability of cellular uptake and RAGE degradation (Table S1, Supporting Information). When the RAP ratio (w/w) in the nanoparticles reached 2%, R_2NP had significantly higher intracellular accumulation in bEnd.3-RAGE cells (**Figure 1A**; Figure S5, Supporting Information), and the RAGE expression was reduced by 1.25 times after treatment with R_8NP (RAP ratio reached 15%) for 24 h (Figure 1B). Hence, R_8NP (nanoparticle composed of full PPR, abbreviated to endoTAC) were considered to afterward inspect targeted protein degradation, the R_3NP (nanoparticle modified with 25% PPR that only had targeting capacity, abbreviated to RNP) and NP (nanoparticle without PPR) were used as the control groups.

Dynamic light scattering (DLS) showed that nanoparticles exhibited similar zeta potential, particle size, and polydispersity index (PDI), while the size of these nanoparticles did not change significantly in PBS, 10% FBS, and 50% FBS within 24 h (Table S2 and Figure S6, Supporting Information; Figure 1C), confirming their good stability. The insignificant hemolysis also indicated the good biosafety of nanoparticles (Figure S7, Supporting Information). Simvastatin-loaded nanoparticles (SV@NP, SV@RNP, and SV@endoTAC), which exhibited a neat circle under transmission electron microscope (TEM), had a 30 nm increase in particle size (Figure 1D,E). The drug loading capacity and encapsulation efficiency of simvastatin in nanoparticles were ≈3% and 50% respectively (Table S3, Supporting Information), and simvastatin could slowly release from the nanoparticles within 48 h for ≈75% (Figure 1F).

2.2. RAGE that Binds to RAP Multivalently was More Often Sorted into Lysosomes for the Degradation

As shown in **Figure 2A**, the change of fluorescence intensity was caused by the competitive binding of FPS-ZM1 to RAGE. It indicated that the targeting ability of RAP-modified nanoparticles was due to the binding of RAP to RAGE, which was a

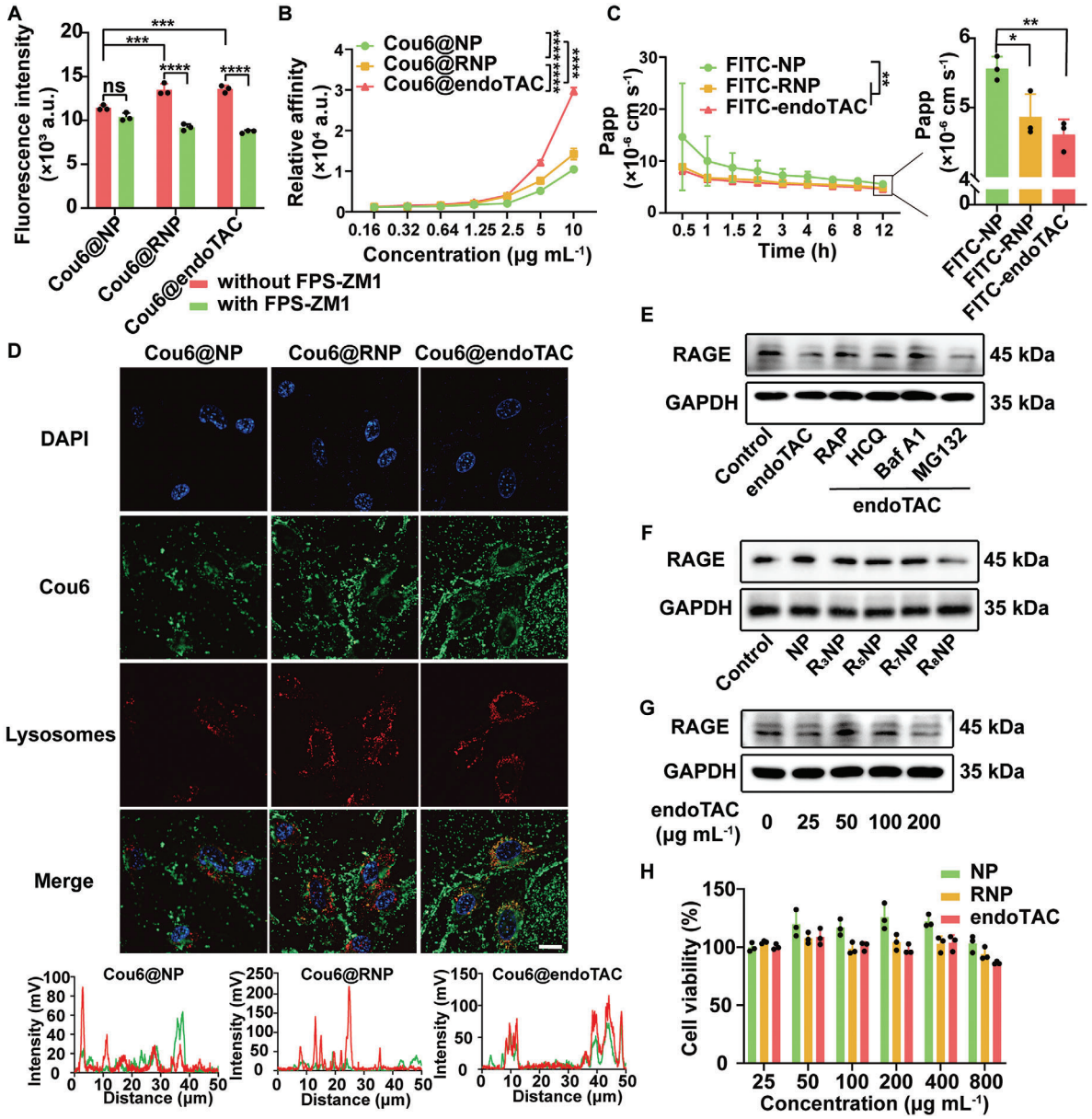

Figure 2. Lysosome-targeting degradation of RAGE by endoTAC. A) Uptake inhibition of nanoparticles measured by flow cytometry after incubated with bEnd.3-RAGE cells for 0.5 h with/without the presence of FPS-ZM1 (5 μM). B) Affinity of nanoparticles to bEnd.3-RAGE cells in serum-free medium. C) Papp of nanoparticles through bEnd.3-RAGE cells at different time points. D) Lysosomal co-localization of nanoparticles after 0.5 h incubation with bEnd.3-RAGE cells, the scale bar represents 20 μm. E) Western blot of RAGE on bEnd.3-RAGE cells after incubated with endoTAC, endoTAC, and RAP (10 μM)/HCQ (20 μM) /Baf A1 (50 nM) /MG132 (proteasome inhibitor, 500 nM) for 24 h. F) Western blot of RAGE on bEnd.3-RAGE cells after incubated with R_nNP for 12 h. G) Western blot of RAGE on bEnd.3-RAGE cells after incubated with different concentrations of endoTAC for 24 h. H) Cytotoxicity of nanoparticles with different concentrations determined by MTT assay. Data are presented as mean ± SD ($n = 3$). Statistical differences were analyzed by one-way ANOVA Dunnett's test and two-way ANOVA Dunnett's test, ns means no significant, $^{*}p < 0.05$, $^{**}p < 0.01$, $^{***}p < 0.001$, and $^{****}p < 0.0001$.

necessary condition for its targeted degradation of RAGE. FITC-labeled nanoparticles were further used to investigate the affinity of nanoparticles to bEnd.3-RAGE cells (Table S4, Supporting Information). The affinity of all three nanoparticles to bEnd.3-RAGE cells varied considerably in both serum-free and complete cell culture medium, with endoTAC having the strongest affinity in all of them, indicating that the cell binding was influenced by RAP density (Figure 2B; Figure S8, Supporting Information). Meanwhile, the retention behavior of endoTAC on BBB was evaluated by apparent permeability coefficient (Papp). The Papp of endoTAC was the lowest at each time point, and it was still 1.2 times lower than NP at the time point of 12 h, even though the difference between the groups gradually narrowed with the extension of time point (Figure 2C). The results of Papp implied endoTAC could stay more on BBB to make a contribution and also reflected the high affinity of endoTAC to

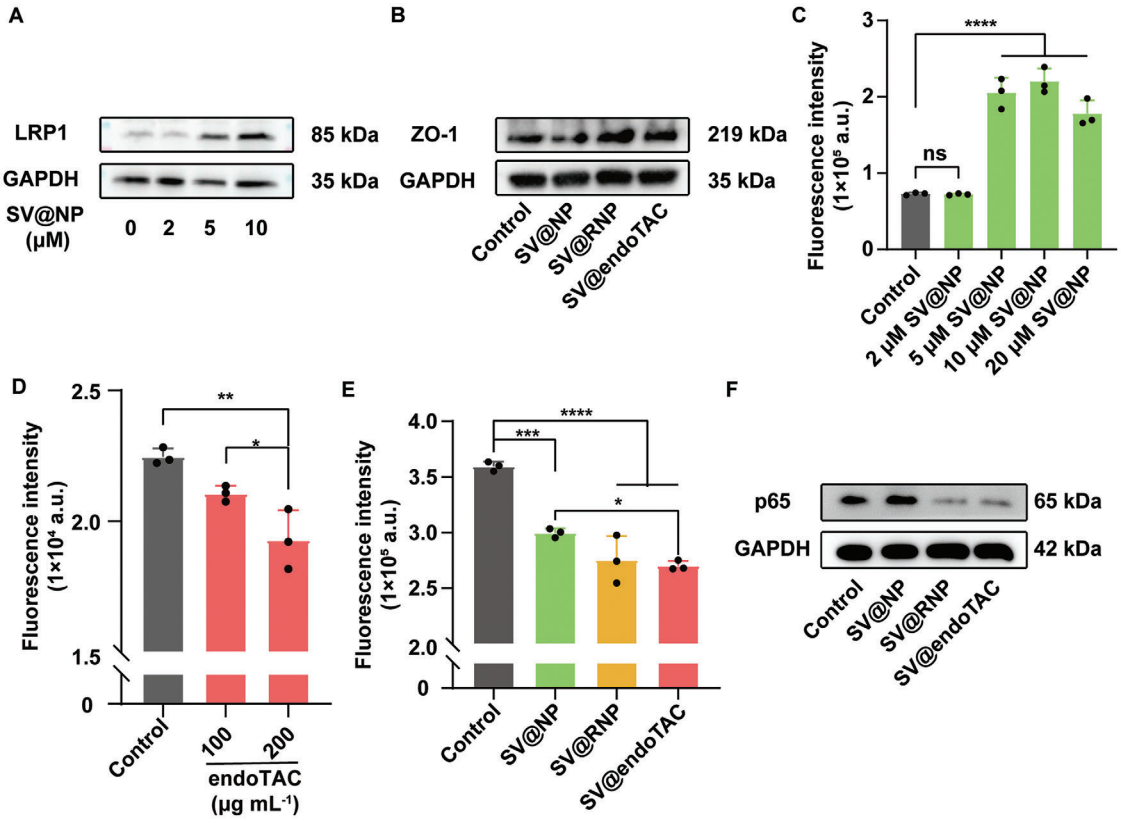

Figure 3. In vitro effect of simvastatin-loaded nanoparticles. A) Western blot of LRP1 on bEnd.3 cells after incubated with SV@NP for 24 h. B) Western blot of ZO-1 on bEnd.3-RAGE cells after incubated with simvastatin-loaded nanoparticles for 24 h. C) FITC-Aβ uptake by bEnd.3 cells after incubated with SV@NP for 24 h measured by flow cytometry. D) FITC-Aβ uptake by bEnd.3-RAGE cells after incubated with endoTAC for 24 h measured by flow cytometry. E) Intracellular ROS in bEnd.3-RAGE cells after incubated with simvastatin-loaded nanoparticles for 24 h measured by flow cytometry using 2′,7′-Dichlorodihydrofluorescein diacetate (DCFH-DA). F) Western blot of NF-κB p65 in bEnd.3-RAGE cells after incubated with simvastatin-loaded nanoparticles for 24 h. Data are presented as mean ± SD ($n = 3$). Statistical differences were analyzed by one-way ANOVA Dunnett's test, ns means no significance, $^{*}p < 0.05$, $^{**}p < 0.01$, $^{***}p < 0.001$, and $^{****}p < 0.0001$.

bEnd.3-RAGE cells laterally. bEnd.3-RAGE cells were also incubated with nanoparticles for multiple time points, afterward the lysosomes were labeled with lysotracker red. Results showed that endoTAC was rapidly and more frequently sorted into lysosomes, and the co-localization phenomenon lasted the longest among the three nanoparticles, indicating the effectiveness of endoTAC in applying sufficient time for RAGE degradation (Figure 2D; Figure S9, Supporting Information). In the presence of free RAP peptides, hydroxychloroquine (HCQ, lysosomal inhibitor), and bafilomycin A1 (Baf A1, lysosomal inhibitor), the RAGE degradation was alleviated (Figure 2E), which further confirmed the targeted degradation of RAGE was driven by the lysosome-related pathway. All of these results advised that RAP in endoTAC bound to RAGE in the polyvalent binding mode, which significantly enhanced its affinity to bEnd.3-RAGE cells, thus increasing sorting of RAGE into lysosomes quickly through endocytosis for its degradation.

Additionally, the ability of endoTAC for RAGE degradation was speedy and concentration-dependent (Figure 2F,G; Figures S10 and S11, Supporting Information), which was consistent with previous studies.[12a,18] Therefore, 100 and 200 μg mL^{-1} nanoparticles that incubated with bEnd.3-RAGE cells for 12/24 h were selected to further verify their therapeutic effect in vitro, for which was non-toxic to cells at these concentrations (Figure 2H).

2.3. SV@endoTAC Restored BBB Integrity to Reduce Aβ Influx, Promote Aβ Efflux, and Decline ROS Level In Vitro

Cobalt chloride ($CoCl_2$) (200 μM) was used to induce LRP1 decrease on bEnd.3 cells in vitro (Figure S12, Supporting Information). LRP1 was effectively lessened by simvastatin at micromolar level (Figure S13, Supporting Information), and it was also considerably upregulated when simvastatin loaded in NP at 5 μM (**Figure 3A**), for which did not exhibit apparent cytotoxicity (Figure S14, Supporting Information). Next, BBB integrity restoring effect of SV@endoTAC was continued to be tested based on the above results, which was verified by tight junction protein (ZO-1) expression on bEnd.3-RAGE cells.[5e,19] As shown in Figure 3B and Figure S15 (Supporting Information), SV@endoTAC had the most obvious ZO-1 up-regulation effect for ≈1.34 times.

Furthermore, Aβ uptake in bEnd.3 cells treated with 5 μM SV@NP was enhanced by 2.81 times (Figure 3C), demonstrating SV@NP could significantly strengthen Aβ efflux owing to the

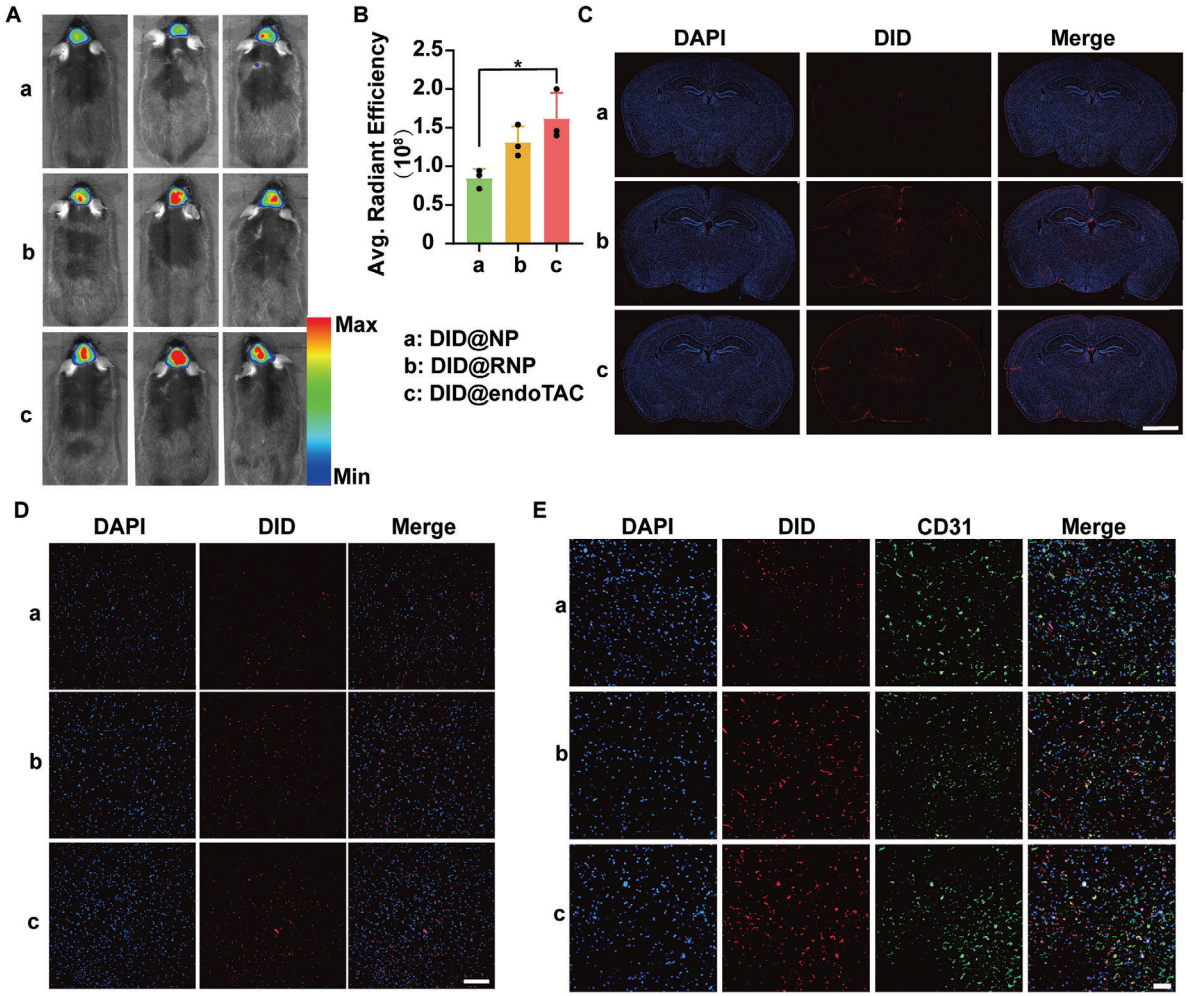

Figure 4. In vivo bio-distribution. A) In vivo fluorescent imaging and B) semi-quantification of FAD^{4T} transgenic mice at 4 h post-tail intravenous injection. The color scale is between 0.4 and 3 × 10^8 [p/s/cm^2/sr]/[μW/cm^2]. C) Fluorescence in whole brain sections of FAD^{4T} transgenic mice, the scale bar represents 2000 μm. D) Fluorescence in cerebral cortex of FAD^{4T} mice, the scale bar represents 100 μm. E) The distribution of nanoparticles in brain vascular cells, the scale bar represents 50 μm. Data are presented as mean ± SD ($n = 3$). Statistical differences were analyzed by one-way ANOVA Dunnett's test, $^*p < 0.05$.

increase of LRP1. In the same way, Aβ uptake in bEnd.3-RAGE cells after incubation with 200 μg mL^{-1} endoTAC exhibited more momentous decrease of ≈22% (Figure 3D; Figure S16, Supporting Information), embodying that endoTAC could diminish Aβ influx in a concentration-dependent manner in keeping with the down-regulation of RAGE. Afterward, ROS level in bEnd.3-RAGE cells after treatment with SV@endoTAC showed the most obvious reduction (31%) of fluorescence intensity (Figure 3E; Figure S17, Supporting Information), suggesting that SV@endoTAC had the best anti-inflammatory property. The anti-inflammatory property of SV@endoTAC was also supported by the decline of p65 in the NF-κB inflammatory pathway (Figure 3F). These results all demonstrated that SV@endoTAC had the better capacity to restore BBB integrity by restituting the normal expression of LRP1 and RAGE, accordingly, could promote Aβ efflux, reduce Aβ influx, minimize neuroinflammation and oxidative stress level.

2.4. In Vivo Distribution

As previously mentioned, RAGE on BBB was pathologically increased in AD model. Consequently, the in vivo distribution was carried out in the FAD^{4T} transgenic mice due to the more pronounced Aβ deposition at younger age, and the experiment was characterized by the DID-labeled nanoparticles (DID@NP, DID@RNP, and DID@endoTAC). First, IVIS Lumina III Imaging System was used to investigate the fluorescence signals of DID in the brain at different time points, and it was found that the fluorescence value reached the highest in a short time (Figure S18, Supporting Information). Therefore, mice injected with DID-labeled nanoparticles for 4 h were further sacrificed to image the brain. As shown in **Figure** 4A,B, RNP and endoTAC had stronger fluorescence signals in the brain than NP, the same results were gained by the whole brain section scan (Figure 4C; Figure S19, Supporting Information). It was also seen that the difference of fluorescence among the three was mainly

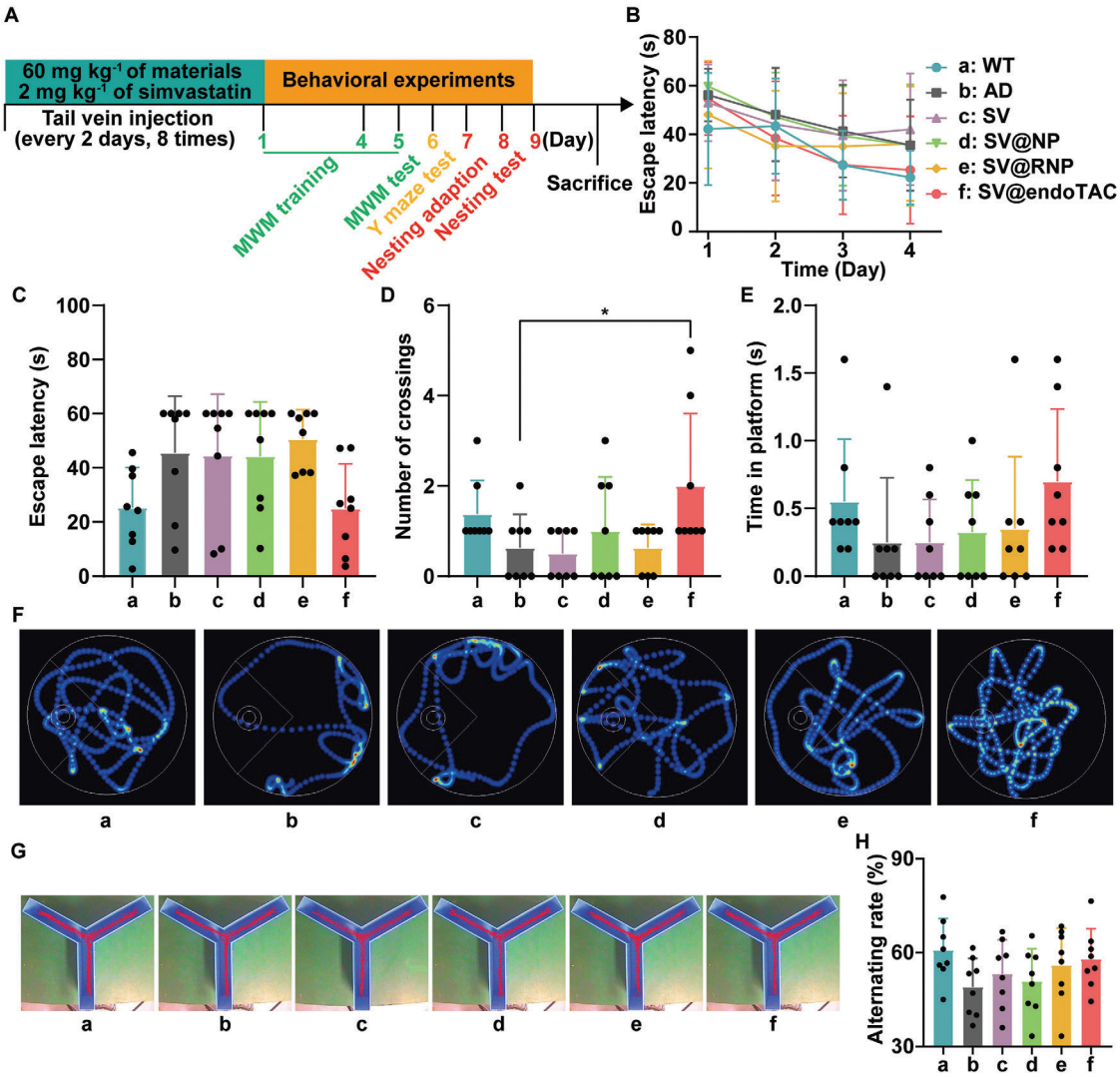

Figure 5. Behavior evaluation was examined by MWM, Y maze, and nesting. A) Schematic diagram of the experimental timeline. B) Escape latencies during the initial training stage of MWM. C) Escape latencies, D) number of platform crossing and E) time in platform during MWM test. F) The representative heat maps of searching paths in MWM. G) The representative trajectories of searching paths in Y maze. H) Autonomous alternation rates for mice in Y maze. Data are presented as mean ± SD ($n = 8$). Statistical differences were analyzed by one-way ANOVA Dunnett's test, $^{*}p < 0.05$.

concentrated in the brain cortex (Figure 4D; Figure S20, Supporting Information). Moreover, endoTAC had the most visible co-localization with vascular cells, while NP hardly co-localized with CD31 (Figure 4E). All of these indicated that RAP modification was useful for the in vivo pathological BBB targeting, and it also reflected the in vivo high BBB retention of endoTAC, which laid a well foundation for therapeutic effects of SV@endoTAC. The fluorescence signals in the liver were strong (Figure S21, Supporting Information), so it was necessary to pay attention to the hepatotoxicity caused by off-target effects. The pharmacokinetic profile of DID@endoTAC showed that the fluorescence signal of DID in blood samples gradually decreased, but remained at a high level at 8 h post-injection. The half-life of DID@endoTAC was determined to be 7.34 h (Figure S22, Supporting Information), which provided the basis for the dosing schedule in the therapeutic trial.

2.5. SV@endoTAC Improved the Behavior of FAD^{4T} Transgenic Mice in Learning and Memory

To evaluate the therapeutic effect of SV@endoTAC for AD, 5-month-old FAD^{4T} transgenic mice were randomly assigned and injected with formulations through the tail vein every two days for totally eight times. After that, Morris water maze (MWM), Y maze, and nesting test were executed to evaluate the ability of SV@endoTAC to improve behaviors in AD mice (**Figure** 5A). In MWM, AD mice treated with SV@endoTAC showed significant learning ability during 4 days training, which was similar as WT mice (Figure 5B). In the space exploration experiment at 5th day, the escape latency of SV@endoTAC treated AD mice was 24.93 ± 16.57 s, which decreased by ≈45% compared with AD mice (45.60 ± 20.90 s) and was similar to WT mice (Figure 5C). Compared with AD group, the crossing and cumulative time to

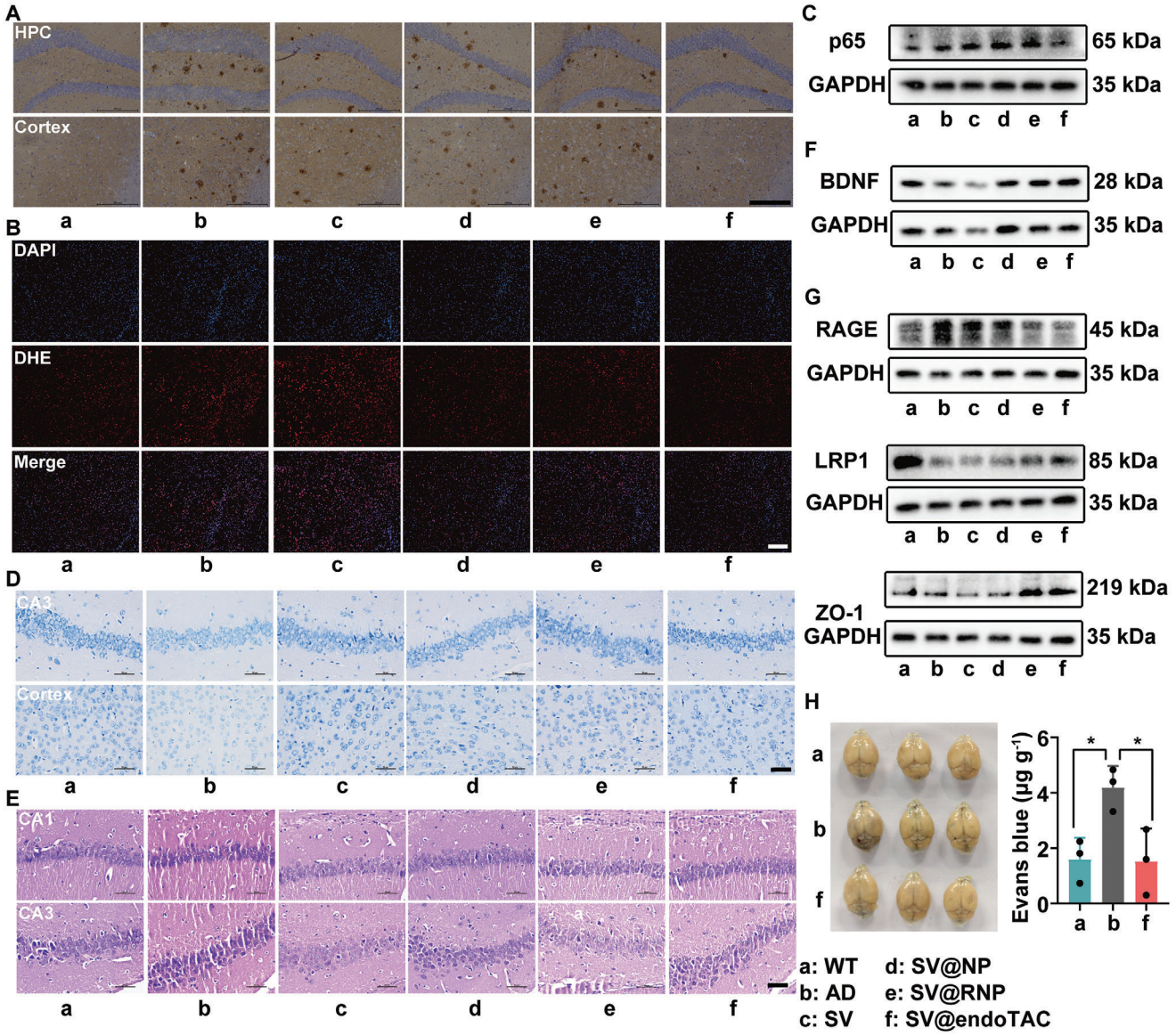

Figure 6. AD lesion microenvironment evaluation after treatment. A) Immunohistochemical staining of Aβ, the scale bar represents 200 μm. B) ROS level shown by DHE staining in the cerebral cortex, the scale bar represents 200 μm. C) Western blot of NF-κB p65 in the brains. D) Nissl staining of brain, the scale bar represents 50 μm. E) HE staining of brain, the scale bar represents 50 μm. F) Western blot of BDNF in the brains. G) Western blot of RAGE, LRP1, and ZO-1 in the brains. H) Images and quantification of Evans blue leakage in the brains, data are presented as mean ± SD ($n = 3$), statistical differences were analyzed by one-way ANOVA Dunnett's test, $^{*}p < 0.05$.

platform of SV@endoTAC group was increased by 3.17 and 2.8 times, respectively (Figure 5D,E; Figure S23, Supporting Information). Further analysis of the swimming trajectories found AD mice had no awareness of actively seeking the platform, while WT mice had the awareness by crossing the platform area back and forth for many times, and SV@endoTAC group remarkably resembled WT mice in trajectory (Figure 5F; Figure S24, Supporting Information). In the Y-maze and nesting experiments, SV@endoTAC group behaved similar to WT mice in the autonomic alternating behavior (Figure 5G,H) and nesting behavior (Figure S25, Supporting Information). All these indicated that SV@endoTAC could rescue the impairment of AD mice in learning and memory to the normal level.

2.6. SV@endoTAC Improved In Vivo AD Lesion Microenvironment

The in vivo therapeutic effect of SV@endoTAC on AD was further evaluated at the biological level. The immunohistochemical staining result suggested that SV@endoTAC could effectively remove toxic protein in the brain by reducing Aβ deposition (**Figure 6A**; Figure S26, Supporting Information). ROS level shown by DHE staining was decreased in a remarkable way after treatment with SV@endoTAC (Figure 6B; Figure S27, Supporting Information). As previous studies mentioned, NF-κB pathway activated by the RAGE-Aβ complex continued to aggravate neuroinflammation, while the representative protein p65 in

NF-κB pathway returned to normal levels in SV@endoTAC group (Figure 6C; Figure S28, Supporting Information). Besides, anti-inflammatory factors IL-10 and TGF-β in brain were significantly enhanced to the normal level (Figure S29, Supporting Information). All results revealed that SV@endoTAC was excellent in effectively relieving oxidative stress and neuroinflammation in the brain.

Neurons were beneficial in learning and memory. According to Nissl staining (Figure 6D), SV@endoTAC reversed the lessening in the number of Nissl bodies and the phenomenon of more vacuolation in AD mice, thus restoring neuronal cells to that of healthy mice, which indicated the neuroprotective effect of SV@endoTAC. HE staining of brain showed SV@endoTAC could repair brain cell morphology (Figure 6E), which was similar as Nissl staining. Moreover, BDNF protein in the brain of AD mice returned to normal level after SV@endoTAC treatment (Figure 6F; Figure S30, Supporting Information), which may be a positive feedback regulation caused by the neuroprotective role of SV@endoTAC, and could also prove the effectiveness of SV@endoTAC in neuroprotection.

We further validated the mechanism by which SV@endoTAC rescued AD pathologies. As expected, western blot assay and its semi-quantification showed that RAGE was significantly down-regulated, LRP1 expression was almost close to that of WT mice, and ZO-1 expression also obviously increased in the cerebral cortex of AD mice after SV@endoTAC treatment (Figure 6G; Figure S31, Supporting Information). Herein, Evans blue dye further substantiated the validity of SV@endoTAC in repairing in vivo BBB function (Figure 6H). These were all consistent with in vitro results, indicating SV@endoTAC could degrade RAGE and increase LRP1 to restore BBB integrity, thereby improving in vivo AD lesion microenvironment.

2.7. In Vivo Transcriptomic Analysis

To investigate the effect of SV@endoTAC on gene level of AD mice, we further analyzed the transcriptomic characteristics of SV@endoTAC treated and untreated AD mice. In the differential gene analysis, SV@endoTAC group shared 1169 up-regulated transcripts (red dots) and 981 down-regulated transcripts (blue dots) with AD group, in which AD risk genes such as *Trem2, Sort, Rhoh, Il34, Inpp5d, Ptk2b, Abi3*, etc. were significantly down-regulated (**Figure** 7A,B).[20] Kyoto Encyclopedia of Genes and Genomes (KEGG) enrichment analysis also found a number of AD-related signaling pathways that had been reported to participate in the development of AD and related inflammatory diseases, such as cGMP-PKG signaling pathway, Wnt signaling pathway, MAPK signaling pathway, mTOR signaling pathway, NF-κB signaling pathway, etc. The enrichment of AGE-RAGE signaling pathway may be related to the targeted degradation strategy of RAGE, ABC transporters, and lysosomes raised also acted essentially in lysosome-targeting protein degradation. In addition, tight junction was discovered to be enriched as before (Figure 7C). Through Gene Ontology (GO) analysis, we found that GO terms of interest were significantly enriched, such as neurogenesis and neurotransmitter, synapses and synaptic signaling, learning and memory, gliogenesis, cell junction, endocytosis and endosome, and protein binding, etc. (Figure 7D). Herein, long-time potentiation, which is closely related to AD,[21] was enriched in both GO and KEGG analyses. Similarly, gene set enrichment analysis (GSEA) showed that NMDA receptors activation, which is involved in long-time potentiation, presented a negative correlation with AD group (Figure 7E).[22] Moreover, differentially expressed genes (DEGs) in the enriched long-time potentiation pathway also revealed some degree of correlation with the genes for the target proteins RAGE and LRP1 by protein–protein interaction networks (PPI networks) in Figure 7F. Taken together, these transcriptomic data provided ample evidences for the effective treatment of SV@endoTAC to AD through the regulation of multiple pathways.

2.8. In Vivo Systemic Toxicity

The body weight of mice was recorded during the treatment, and there was no obvious trend of weight loss (Figure S32, Supporting Information). After the treatment, the heart, liver, spleen, lung, and kidney of mice were taken for HE staining, which demonstrated no significant differences for each group of mice (Figure S33, Supporting Information). The blood routine parameters showed that there were no obvious peripheral abnormalities in each group (Figure S34, Supporting Information). Blood biochemistry showed that the nanoparticles did not cause significant hepatotoxicity and nephrotoxicity in each group (Figure S35, Supporting Information). In summary, simvastatin-loaded nanoparticles used in this study has marvelous biosafety and compatibility.

3. Conclusion

TPD strategy interferes with protein expression function by taking advantage of the inherent protein degradation mechanism, which controls protein homeostasis. Except to the most widely employed proteolysis-targeting chimeras, lysosome-targeting protein degradation technology has been developed rapidly in recent years to expand the range of proteins of interest, for which is expected to be beneficial in a variety of diseases by degrading proteins that are abnormally aggregated or upregulated. Undoubtedly, the lysosome-targeting protein degradation technology fills the gap of drug-free therapeutic proteins or provides new therapeutic approaches based on drug therapy. Herein, in response to the abnormally upregulated RAGE on pathological BBB, we designed a lysosomal-shuttling nano-chimeras (endoTAC) to treat AD by RAGE degradation. The system utilized the polyvalent combination between RAP and RAGE to achieve more lysosomal sorting of RAGE for its degradation, which was manifested in the high affinity of the system to pathological BBB. Meanwhile, simvastatin loaded in the system (SV@endoTAC) was combined to upregulate the damaged LRP1. Through the down-regulation of RAGE and the up-regulation of LRP1 to restore pathological BBB, the system reversed brain homeostasis defects of AD. In conclusion, SV@endoTAC has achieved the application of lysosome-targeting protein degradation technology in AD treatment, and the lysosomal-shutting nano-chimeras may be applicative to various diseases by the degradation of pathological proteins.

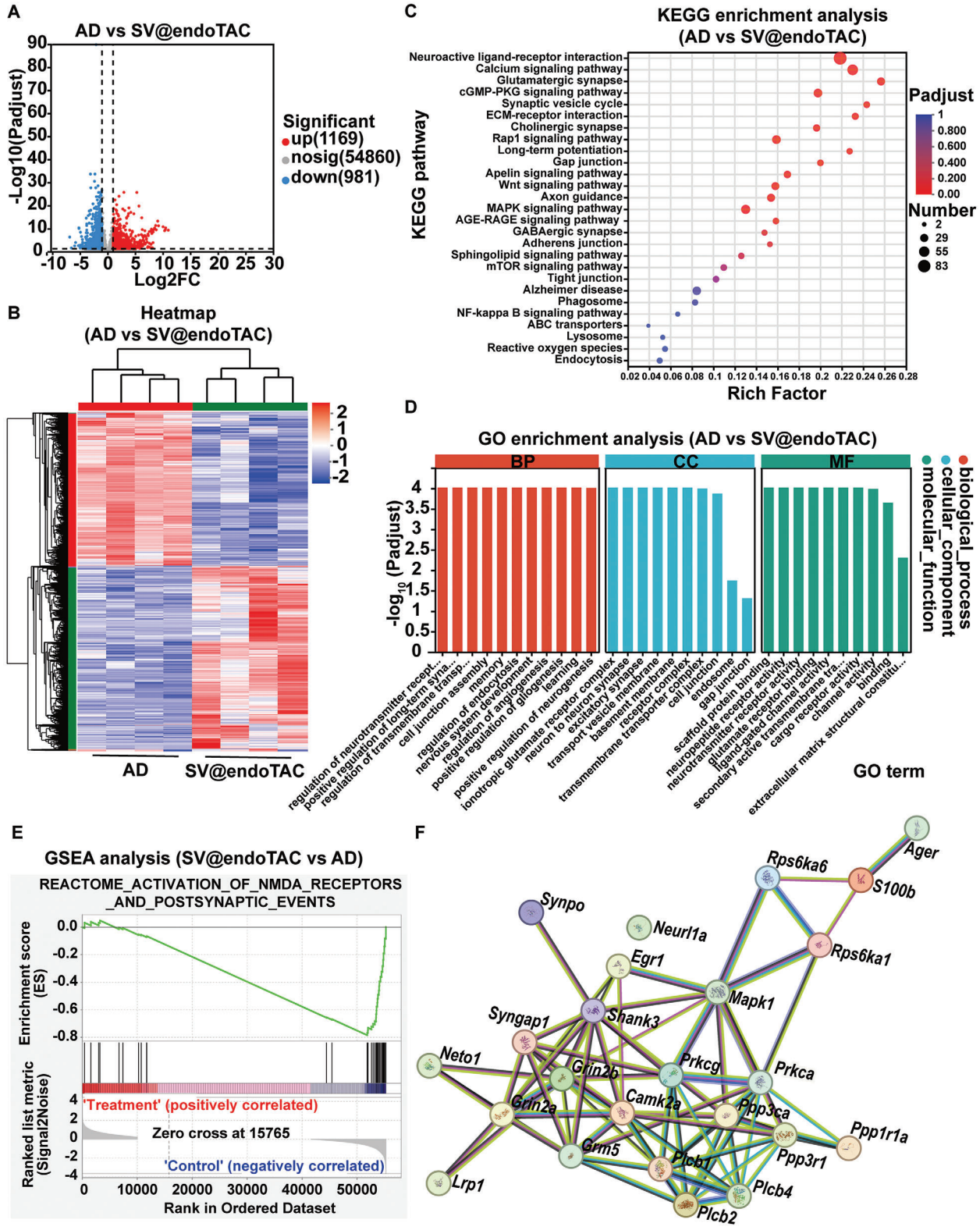

Figure 7. In vivo transcriptomics analysis of FAD^{4T} transgenic mice brains after therapy. A) Volcano map of DEGs between AD and SV@endoTAC group ($p < 0.05$, |fold change| ≥ 2). B)Heat map of DEGs in AD and SV@endoTAC group. C) KEGG pathway enrichment analysis of DEGs between AD and SV@endoTAC group. D) Bar plot of GO enrichment analysis of genes between AD and SV@endoTAC group. Biological process, BP; Molecular function, MF; Cell component, CC. E) GSEA results for the activation of NMDA receptors. F) PPI networks between DEGs in the enriched long-time potentiation pathway and the targeted genes (created by cn.string-db.org).

4. Experimental Section

Materials: $PLGA_{5000}$-PEG_{2000}-FITC, $PLGA_{5000}$-PEG_{2000}-MAL, $PLGA_{5000}$-$mPEG_{2000}$, and $PLGA_{5000}$-$mPEG_{5000}$ were purchased from Guangzhou Tanshtech Co., Ltd (Guangzhou, China), and the lactide/ethyl lactide of PLGA is 50/50. CELKVLMEKEL peptide chain was synthesized by Sangon Biotech Co., Ltd (Shanghai, China). Simvastatin was obtained from Energy Chemical (Shanghai, China). Coumarin-6 was purchased from Sigma (USA). DID was purchased from Biotium (USA). Amyloid-β (1-42) peptide ($A\beta_{1\text{-}42}$) and FITC-amyloid-β (1-42) peptide (FITC-$A\beta_{1\text{-}42}$) were synthesized by GL Biochem Ltd. (Shanghai, China). Dulbecco's modified Eagle's medium (DMEM) was purchased from Gibco (USA). Fetal bovine serum (FBS) was obtained from ABW (USA). DCFH-DA was obtained from Bide Pharmatech Co., Ltd. (Shanghai, China). Evans blue was obtained from Meilunbio (Dalian, China).

Cell Lines and Animals: bEnd.3 cells were gained from the Chinese Academy of Science Cells Bank (Shanghai, China). bEnd.3 cells overexpressing RAGE were constructed by anti-hela biological technology trade Co., Ltd (Xiamen, China). Cells were maintained in DMEM supplemented with 10% FBS and 1% penicillin-streptomycin, and incubated at 37 °C under 5% CO_2. Male wild-type C57 and Kunming mice were provided by SiPeiFu Biotechnology Co., Ltd. (Beijing, China). Male FAD^{4T} [*B6/JGpt-Tg(Thy-APP/Thy-PSEN1)5/ Gpt*] mice were furnished by the GemPharmatech Co., Ltd (Jiangsu, China). All animal experiments were in accordance with animal experimental ethics approved by Sichuan University (KS2020420).

Antibodies: The anti-RAGE (A13264, 1:1000 dilution for WB), anti-GAPDH (AC001, 1:100000 dilution for WB), anti-BDNF (A18129, 1:5000 dilution for WB) antibodies, horseradish peroxidase-conjugated secondary antibodies goat anti-rabbit (AS014, 1:10000 dilution for WB) and goat anti-mouse (AS003, 1:10000 dilution for WB) were purchased from ABclonal Technology Co., Ltd. (Wuhan, China). The DYKDDDDK tag (66008-4-Ig, 1:3000 dilution for WB, binds to FLAG tag epitope) and anti-ZO-1 (21773-1-AP, 1:5000 dilution for WB) antibodies were purchased from Proteintech Group, Inc. (Wuhan, China). The anti-LRP1 (ab92544, 1:5000 dilution for WB), anti-$A\beta_{1\text{-}42}$ (ab201060, 1:1000 for immunohistochemistry), and anti-CD31 (ab222783, 1:100 dilution for immunofluorescent staining) antibodies were purchased from Abcam (UK). The anti-NF-κB p65 antibody (D14E12, 1:1000 dilution for WB) was purchased from Cell Signaling Technology, Inc. (USA).

Preparation and of SV@NP, SV@RNP and SV@endoTAC: The nanoparticles were prepared by ultrasonic dispersion. $PLGA_{5000}$-$mPEG_{5000}$ (10 mg mL^{-1}, 0.4 mL) and simvastatin (10 mg mL^{-1}, 20 µL) were separately dissolved in the mixed organic solvent (acetonitrile: DMSO = 3:1) and DMSO, and then gradually added to UP water (4 mL) to ultrasonication (JY92-IIN, SCITNEZ, Ningbo). The solution was evaporated using a rotary evaporator to remove the organic phase, further centrifuged to remove impurities, and then concentrated by ultrafiltration to obtain SV@NP. The preparation of SV@RNP and SV@endoTAC were same to above, in addition to replace $PLGA_{5000}$-$mPEG_{5000}$ with $PLGA_{5000}$-$mPEG_{2000}$ (7 mg mL^{-1}, 310 µL) and PPR (8.3 mg mL^{-1}, 90 µL) to prepare SV@RNP, or PPR (8.3 mg mL^{-1}, 400 µL) to prepare SV@endoTAC. NP, RNP, and endoTAC were prepared similarly to the method above, except without simvastatin. The preparation of Cou6/DID/FITC-labeled nanoparticles was also resemble to simvastatin-loaded nanoparticles, except that the simvastatin solution was replaced with Cou6 (0.5/1 mg mL^{-1}) or DID (1 mg mL^{-1}) or $PLGA_{5000}$-PEG_{2000}-FITC (20 mg mL^{-1}) solution.

Characterization of Nanoparticles: The hydrodynamic particle size and zeta potential of nanoparticles were detected by DLS (Zetasizer Nano ZS90, Brookhaven, USA), the morphology of nanoparticles was characterized by TEM (HT7800, Hitachi, Shanghai). The stability of nanoparticles was investigated in PBS, 10% FBS, and 50% FBS. The drug loading capacity and encapsulation efficiency of simvastatin were further determined by the UV–vis spectrophotometer (GENESYS 180, Thermo Scientific, USA) at 246 nm. The cumulative release of simvastatin was measured by the dialysis method. Simply, simvastatin-loaded nanoparticles (4 mg mL^{-1}, 0.9 mL) were placed in a dialysis bag (MWCO = 1000 Da) and dialyzed against 10 mM PBS (10 mL) containing 0.5% tween-80 at pH 7.4. The dialysate at different times was withdrawn for HPLC (LC-20A, Shimadzu, Japan) analysis. The HPLC test conditions were as follows: Diamonsil C18 (2) 5 µm, 250 × 4.6 mm (chromatographic column); Acetonitrile/0.1 M phosphate = 90/10 (mobile phase 1); Acetonitrile/0.1 M phosphate = 80/20 (mobile phase 2); 1 mL min^{-1} (flow rate); 30 °C (column temperature); 238 nm (UV detection wavelength).

Cell Uptake: bEnd.3-RAGE cells were planted in 12-well plates at a density of 5 × 10^4 per well and grew to ≈80%, then the Cou6-labeled nanoparticles (50 µg mL^{-1}) were added or Cou6-labeled nanoparticles and FPS-ZM1 (5 µM) were simultaneously added to incubate for 0.5 h, then cells were treated to detect the fluorescence of Cou6 by flow cytometry (NovoCyt, Agilent, USA). 1 × 10^5 bEnd.3-RAGE cells were plated onto glass slides and grew to ≈80%. Cells were stained with DAPI for 5 min to label the nuclei and further fixed with 4% paraformaldehyde after incubated with Cou6-labeled nanoparticles for 0.5 h, and the fluorescence of Cou6 was observed by CLSM (DMi8, Leica, Germany).

West Blot: bEnd.3-RAGE cells were seeded in 6-well plates at a density of 3 × 10^5 per well and pre-cultured by $A\beta_{1\text{-}42}$ oligomer (5 µM) for 24 h, next incubated with nanoparticles and other preparations for 24 h. bEnd.3 cells were seeded in 6-well plates at a density of 5 × 10^4 per well and grew to ≈80%, then incubated with nanoparticles and other preparations for 24 h to finish the experiments. The total proteins of cells were extracted by cell lysate, quantified by BCA and diluted in loading buffer. Proteins (20–100 µg) were isolated in SDS-PAGE and subsequently transferred to the PDVF membrane. After blocked by skimmed milk, the PDVF membrane was first bound to the primary antibody of target protein, therewith incubated with the horseradish peroxidase-conjugated secondary antibody, and finally imaged by Chemiluminescence imaging System (ChemiDoc XRS$^+$, Bio-Rad, USA).

BBB Retention: bEnd.3-RAGE cells were spread in the upper chamber of transwell at a density of 2 × 10^4 per well, and resistance detector was used to assess the transmembrane resistance value of cells every day. The experiment was carried out when there was no significant difference between the resistance values of the two measurements. FITC-labeled nanoparticles were diluted to 0.4 mg mL^{-1} with Hank's Balanced Salt Solution and added to the upper chamber of transwell. The fluorescence intensity in the lower chamber at 0.5, 1, 2, 4, 6, 8, and 12 h was measured to calculate Papp of the nanoparticles.

Regulation of Aβ Transport: bEnd.3 cells were laid on 12-well plates at a density of 1 × 10^5 per well. When the cells grew to ≈80%, cells were incubated with SV@NP in culture medium containing $CoCl_2$ (200 µM) for 24 h, afterward with FITC-$A\beta_{1\text{-}42}$ (1 µM) for 1 h. The fluorescence of FITC was collected by flow cytometry to represent $A\beta_{1\text{-}42}$ content. Similarly, bEnd.3-RAGE cells were seeded in 12-well plates at a density of 1×10^5 per well, and pre-incubated with $A\beta_{1\text{-}42}$ oligomer for 24 h, further with endoTAC for 24 h, and finally with FITC-$A\beta_{1\text{-}42}$ for 1 h. The fluorescence of FITC was also tested by flow cytometry.

Intracellular ROS Scavenging: bEnd.3 cells were planted 1 × 10^5 per well, pre-incubated with $A\beta_{1\text{-}42}$ oligomer and $CoCl_2$ for 24 h. Subsequently, the cells were incubated with SV@NP in different concentrations or simvastatin-loaded nanoparticles (5 µM simvastatin, 200 µg mL^{-1} material) for 24 h respectively, and finally with DCFH-DA (10 µM) for 0.5 h. The fluorescence was analyzed by flow cytometry to evaluate the anti-inflammatory effects of nanoparticles.

Affinity Assay: The affinity determination method was referred to previous studies.[8a,b] Generally, bEnd.3-RAGE cells were planted in 12-well plates at a density of 1 × 10^5 per well, pre-incubated with $A\beta_{1\text{-}42}$ oligomer for 24 h. Then cells were incubated with Cou6-labled nanoparticles in serum-free or containing medium for 90 min at 4 °C to collect the fluorescence by flow cytometry.

Co-Localization with Lysosomes: bEnd.3-RAGE cells were covered onto glass slides at a density of 1 × 10^5 per well, and pre-incubated with $A\beta_{1\text{-}42}$ oligomer for 24 h. Furthermore, cells were incubated with Cou6-labled nanoparticles followed with lysotracker red DND99 (50 nM) for 1 h. Eventually, cells were stained with DAPI for 5 min to label the nuclei and further fixed with 4% paraformaldehyde to observe the co-localization between nanoparticles and lysosomes by CLSM.

In Vivo Distribution: DID-labled nanoparticles (0.25 mg kg^{-1} DID) were injected intravenously into 7-month-old FAD^{4T} transgenic mice. After 4 h, the in vivo fluorescence intensity of mice was determined. Then, mice were sacrificed to collect major organs and image ex vivo. The brains were fixed in 4% paraformaldehyde for 24 h, dehydrated in 15% (w/v), and 30% sucrose solution for 24 h in turn, followed by frozen sections. The sections were stained with CD31 and DAPI to show nuclei and were immediately observed by CLSM.

Treatment Options: The 5-month-old FAD^{4T} transgenic mice were randomly divided into five groups: AD, SV, SV@NP, SV@RNP, SV@endoTAC, and the WT *C57BL/6* mice were used as healthy control group. Nanoparticles with simvastatin (2 mg kg^{-1}) and the materials (60 mg kg^{-1}, based on SV@NP) were injected intravenously once every two days for a total of eight sessions. Simvastatin was taken orally.

MWM Test: The MWM test was used to evaluate the learning and long-term memory ability of mice. The pool with a diameter of 120 cm was divided into four quadrants, and black markers of different shapes were affixed to the center of wall in each quadrant. One of the four quadrants was selected as the target quadrant, in which a circular platform (8 cm in diameter and 20 cm in height) was placed for the mice to find. The water level was ≈1.5 cm higher than the platform in the target quadrant, and the water temperature was maintained at ≈20 °C. The EthoVision XT system was used to record the behavior of mice. In the first four days of the navigation test, the mice were placed in the water from the remaining three quadrants except the target quadrant each day, and the time it took them to find the platform hidden under the water surface was recorded, which was called the escape latency. On 5th day of the space exploration experiment, the platform was removed, and mice were placed into the pool in one quadrant to note their swimming track within 60 s. The latency of mice found the original platform for the first time, the times of mice crossed the target platform, the accumulated time in the platform area, and the movement trajectory were recorded.

Y Maze Test: The Y maze test was used to evaluate the short-term memory ability of mice. The Y maze is a Y-shaped experimental device composed of three identical arms at 120° to each other, with each arm 130 mm long, 65 mm wide, and 60 mm high. The mice were placed into the Y maze from one arm finally, and the EthoVision XT system was used to record the exploration behavior of the mice in the Y maze within 5 min to further calculate the autonomous alternation rate.

Evans Blue In Vivo Assay: After the treatment, mice were intravenously injected with 2% Evans blue solution (200 μg g^{-1}). 3 h later, the mice were anesthetized, and the brains were dissected after myocardial perfusion with cold PBS and photographed. To quantify Evans blue leakage, the brains were further homogenized in 50% trichloroacetic acid (200 mg in 600 μL) and centrifuged at 13 000 rpm for 20 min. The supernatant was measured at an optical density of 610 nm (OD610).[23]

Statistical Analysis: All data were presented as mean ± standard deviation (s.d.). The statistical difference between experimental results was assessed by one-way ANOVA Dunnett's test and two-way ANOVA Dunnett's test. *p*-value lower than 0.05 was considered statistically significant. Statistical analysis was carried out using GraphPad Prism 8.

Supporting Information

Supporting Information is available from the Wiley Online Library or from the author.

Acknowledgements

The work was supported by the following fundings:111 Project (B18035, China), National Natural Science Foundation of China (No.82373801, China).

Conflict of Interest

The authors declare no conflict of interest.

Data Availability Statement

The data that support the findings of this study are available in the supplementary material of this article.

Keywords

Alzheimer's disease, BBB repairment, lysosome-targeting protein degradation, nano-delivery system, polyvalent binding

Received: July 29, 2024
Revised: December 2, 2024
Published online: December 17, 2024

[1] D. S. Knopman, H. Amieva, R. C. Petersen, G. Chetelat, D. M. Holtzman, B. T. Hyman, R. A. Nixon, D. T. Jones, *Nat. Rev. Dis. Primers* **2021**, *7*, 33.

[2] a) *AAIC2021, Alzheimer's Dementia* **2021**, *17*, 1868; b) S. Long, C. Benoist, W. Weidner, in *Alzheimer's Dis. Int*, Alzheimer's Disease International, London, England **2023**.

[3] a) E. Joe, J. M. Ringman, *BMJ* **2019**, *367*, l6217; b) J. Cummings, Y. Zhou, G. Lee, K. Zhong, J. Fonseca, F. Cheng, *Alzheimer's Dementia: Trans. Res. Clin. Interv.* **2023**, *9*, e12385.

[4] a) J. M. Long, D. M. Holtzman, *Cell* **2019**, *179*, 312; b) K. Tam, Y. Ju, *Neural Regener. Res.* **2022**, *17*, 543; c) T. Guo, D. Zhang, Y. Zeng, T. Y. Huang, H. Xu, Y. Zhao, *Mol. Neurodegenerat.* **2020**, *15*, 40.

[5] a) A. Montagne, Z. Zhao, B. V. Zlokovic, *J. Exp. Med.* **2017**, *214*, 3151; b) D. Wang, F. Chen, Z. Han, Z. Yin, X. Ge, P. Lei, *Front. Cel. Neurosci.* **2021**, *15*, 695479; c) M. I. Alvarez-Vergara, A. E. Rosales-Nieves, R. March-Diaz, G. Rodriguez-Perinan, N. Lara-Ureña, C. Ortega-de San Luis, M. A. Sanchez-Garcia, M. Martin-Bornez, P. Gómez-Gálvez, P. Vicente-Munuera, B. Fernandez-Gomez, M. A. Marchena, A. S. Bullones-Bolanos, J. C. Davila, R. Gonzalez-Martinez, J. L. Trillo-Contreras, A. C. Sanchez-Hidalgo, R. del Toro, F. G. Scholl, E. Herrera, M. Trepel, J. Körbelin, L. M. Escudero, J. Villadiego, M. Echevarria, F. de Castro, A. Gutierrez, A. Rabano, J. Vitorica, A. Pascual, *Nat. Commun.* **2021**, *12*, 3098; d) K. Kisler, A. R. Nelson, A. Montagne, B. V. Zlokovic, *Nat. Rev. Neurosci.* **2017**, *18*, 419; e) B. V. Zlokovic, *Neuron* **2008**, *57*, 178.

[6] a) J. E. Donahue, S. L. Flaherty, C. E. Johanson, J. A. Duncan, G. D. Silverberg, M. C. Miller, R. Tavares, W. Yang, Q. Wu, E. Sabo, V. Hovanesian, E. G. Stopa, *Acta Neuropathol.* **2006**, *112*, 405; b) S. D. Yan, X. Chen, J. Fu, M. Chen, H. Zhu, A. Roher, T. Slattery, L. Zhao, M. Nagashima, J. Morser, A. Migheli, P. Nawroth, D. Stern, A. M. Schmidt, *Nature* **1996**, *382*, 685; c) R. Deane, S. Du Yan, R. K. Submamaryan, B. LaRue, S. Jovanovic, E. Hogg, D. Welch, L. Manness, C. Lin, J. Yu, H. Zhu, J. Ghiso, B. Frangione, A. Stern, A. M. Schmidt, D. L. Armstrong, B. Arnold, B. Liliensiek, P. Nawroth, F. Hofman, M. Kindy, D. Stern, B. Zlokovic, *Nat. Med.* **2003**, *9*, 907; d) E. Cuevas, H. Rosas-Hernandez, S. M. Burks, M. A. Ramirez-Lee, A. Guzman, S. Z. Imam, S. F. Ali, S. Sarkar, *Metabol. Brain Dis.* **2019**, *34*, 1365.

[7] a) Y. Ding, D. Xing, Y. Fei, B. Lu, *J. Am. Chem. Soc.* **2022**, *51*, 8832; b) L. Zhao, J. Zhao, K. Zhong, A. Tong, D. Jia, *Signal Trans. Target. Ther.* **2022**, *7*, 113.

[8] a) J. Zheng, W. He, J. Li, X. Feng, Y. Li, B. Cheng, Y. Zhou, M. Li, K. Liu, X. Shao, J. Zhang, H. Li, L. Chen, L. Fang, *J. Am. Chem. Soc.* **2022**, *144*, 21831; b) C. Zhu, W. Wang, Y. Wang, Y. Zhang, J. Li, *Angew. Chem., Int. Ed.* **2023**, *62*, 202300694; c) G. Ahn, N. M. Riley, R. A. Kamber, S. Wisnovsky, S. Moncayo von Hase, M. C. Bassik, S. M. Banik, C. R. Bertozzi, *Science* **2023**, *382*, eadf6249; d) S. M. Banik, K. Pedram,

S. Wisnovsky, G. Ahn, N. M. Riley, C. R. Bertozzi, *Nature* **2020**, *584*, 291.

[9] M. F. Coutinho, M. J. Prata, S. Alves, *Mol. Genet. Metab.* **2012**, *107*, 257.

[10] a) E. Magdalena Estirado, M. A. Aleman Garcia, J. Schill, L. Brunsveld, *J. Am. Chem. Soc.* **2019**, *141*, 18030; b) C. M. Csizmar, J. R. Petersburg, T. J. Perry, L. Rozumalski, B. J. Hackel, C. R. Wagner, *J. Am. Chem. Soc.* **2018**, *141*, 251.

[11] a) M. Mammen, S.-K. Choi, G. M. Whitesides, *Angew. Chem., Int. Ed.* **1998**, *37*, 2754; b) A. Conway, T. Vazin, D. P. Spelke, N. A. Rode, K. E. Healy, R. S. Kane, D. V. Schaffer, *Nat. Nanotechnol.* **2013**, *8*, 831; c) C. Fasting, C. A. Schalley, M. Weber, O. Seitz, S. Hecht, B. Koksch, J. Dernedde, C. Graf, E.-W. Knapp, R. Haag, *Angew. Chem., Int. Ed.* **2012**, *51*, 10472; d) X. Montet, M. Funovics, K. Montet-Abou, R. Weissleder, L. Josephson, *J. Med. Chem.* **2006**, *49*, 6087.

[12] a) J. Niewoehner, B. Bohrmann, L. Collin, E. Urich, H. Sade, P. Maier, P. Rueger, J. O. Stracke, W. Lau, A. C. Tissot, H. Loetscher, A. Ghosh, P.-O. Freskgård, *Neuron* **2014**, *81*, 49; b) N. Bien-Ly, Y. J. Yu, D. Bumbaca, J. Elstrott, C. A. Boswell, Y. Zhang, W. Luk, Y. Lu, M. S. Dennis, R. M. Weimer, I. Chung, R. J. Watts, *J. Exp. Med.* **2014**, *211*, 233.

[13] A. P. Tolstova, A. A. Adzhubei, V. A. Mitkevich, I. Y. Petrushanko, A. A. Makarov, *Int. J. Mol. Sci.* **2022**, *23*, 11816.

[14] a) S. E. Storck, S. Meister, J. Nahrath, J. N. Meißner, N. Schubert, A. Di Spiezio, S. Baches, R. E. Vandenbroucke, Y. Bouter, I. Prikulis, C. Korth, S. Weggen, A. Heimann, M. Schwaninger, T. A. Bayer, C. U. Pietrzik, *J. Clin. Invest.* **2015**, *126*, 123; b) Y.-L. Zhang, J. Wang, Z.-N. Zhang, Q. Su, J.-H. Guo, *Neural Regener. Res.* **2022**, *17*, 2355.

[15] a) Y. Yamazaki, N. Zhao, T. R. Caulfield, C.-C. Liu, G. Bu, *Nat. Rev. Neurol.* **2019**, *15*, 501; b) Z. Zhao, A. P. Sagare, Q. Ma, M. R. Halliday, P. Kong, K. Kisler, E. A. Winkler, A. Ramanathan, T. Kanekiyo, G. Bu, N. C. Owens, S. V. Rege, G. Si, A. Ahuja, D. Zhu, C. A. Miller, J. A. Schneider, M. Maeda, T. Maeda, T. Sugawara, J. K. Ichida, B. V. Zlokovic, *Nat. Neurosci.* **2015**, *18*, 978.

[16] J. N. Rauch, G. Luna, E. Guzman, M. Audouard, C. Challis, Y. E. Sibih, C. Leshuk, I. Hernandez, S. Wegmann, B. T. Hyman, V. Gradinaru, M. Kampmann, K. S. Kosik, *Nature* **2020**, *580*, 381.

[17] a) Q. Guo, Q. Zhu, T. Miao, J. Tao, X. Ju, Z. Sun, H. Li, G. Xu, H. Chen, L. Han, *J. Controlled Release* **2019**, *303*, 117; b) M. Zandl-Lang, E. Fanaee-Danesh, Y. Sun, N. M. Albrecher, C. C. Gali, I. Čančar, A. Kober, C. Tam-Amersdorfer, A. Stracke, S. M. Storck, A. Saeed, J. Stefulj, C. U. Pietrzik, M. R. Wilson, I. Björkhem, U. Panzenboeck, *Biochim. Biophys. Acta, Mol. Cell Biol. Lipids* **2018**, *1863*, 40.

[18] T. Wang, L. Sun, T. Ren, M. Hou, Y. Long, J.-H. Jiang, J. He, *Nano Lett.* **2023**, *23*, 9571.

[19] D. Wang, F. Chen, Z. Han, Z. Yin, X. Ge, P. Lei, *Front. Cell. Neurosci.* **2021**, *15*, 695479.

[20] a) H. Holstege, M. Hulsman, C. Charbonnier, B. Grenier-Boley, O. Quenez, D. Grozeva, J. G. J. van Rooij, R. Sims, S. Ahmad, N. Amin, P. J. Norsworthy, O. Dols-Icardo, H. Hummerich, A. Kawalia, P. Amouyel, G. W. Beecham, C. Berr, J. C. Bis, A. Boland, P. Bossù, F. Bouwman, J. Bras, D. Campion, J. N. Cochran, A. Daniele, J.-F. Dartigues, S. Debette, J.-F. Deleuze, N. Denning, A. L. DeStefano, et al., *Nat. Genet.* **2022**, *54*, 1786; b) C. R. Jack, *Lancet Neurol.* **2022**, *21*, 866.

[21] Z. Ismail, B. Creese, D. Aarsland, H. C. Kales, C. G. Lyketsos, R. A. Sweet, C. Ballard, *Nat. Rev. Neurol.* **2022**, *18*, 131.

[22] a) A.-K. Abbas, A. Villers, L. Ris, *Rev. Neurosci.* **2015**, *26*, 507; b) J. P. Dupuis, O. Nicole, L. Groc, *Neuron* **2023**, *111*, 2312; c) X. Yang, R. Gong, L. Qin, Y. Bao, Y. Fu, S. Gao, H. Yang, J. Ni, T.-F. Yuan, W. Lu, *Cell Rep.* **2022**, *40*, 111217.

[23] a) B. Polis, V. Gurevich, M. Assa, A. O. Samson, *Int. J. Mol. Sci.* **2019**, *20*, 4616; b) S. N. Tabatabaei, H. Girouard, A.-S. Carret, S. Martel, *J. Controlled Release* **2015**, *206*, 49; c) C. Wei, W. Jiang, R. Wang, H. Zhong, H. He, X. Gao, S. Zhong, F. Yu, Q. Guo, L. Zhang, L. D. J. Schiffelers, B. Zhou, M. Trepel, F. I. Schmidt, M. Luo, F. Shao, *Nature* **2024**, *629*, 893.